



# Real-time 3D imaging with Fourier-domain algorithms and matrix arrays applied to non-destructive testing

M. Marmonier<sup>a,\*</sup>, S. Robert<sup>a</sup>, J. Laurent<sup>a</sup>, C. Prada<sup>b</sup>

<sup>a</sup> Université Paris-Saclay, CEA, List, F-91120, Palaiseau, France

<sup>b</sup> Institut Langevin, ESPCI Paris, CNRS, PSL University, 75238, Paris, France

## ARTICLE INFO

### Keywords:

Non-destructive testing  
Ultrasonic matrix array  
3D imaging  
Real-time reconstruction  
Fourier-domain algorithms  
Additive manufacturing

## ABSTRACT

Real-time 3D ultrasound imaging with matrix arrays remains a challenge in Non-Destructive Testing (NDT) due to the time-consuming reconstruction algorithms based on delay-and-sum operations. Other algorithms operating in the Fourier domain have lower algorithmic complexities and therefore higher frame rates at the cost of more storage space, which may limit the number of reconstruction points. In this paper, we present an implementation for real-time 3D imaging of the Total Focusing Method (TFM) and the Plane Wave Imaging (PWI), as well as of their Fourier-domain counterparts, referred to as k-TFM and k-PWI. For both types of acquisition, the Fourier-domain algorithms are used to increase frame rates, and they are compared to the time-domain TFM and PWI in terms of image quality, frame rates and memory requirements. In order to greatly reduce their memory requirements, a new implementation of k-TFM and k-PWI is proposed. The four imaging methods are then evaluated by imaging in real time a block of stainless steel containing a 3D network of spherical porosities produced by additive layer manufacturing using a powder bed laser fusion process.

## 1. Introduction

Nowadays, real-time 2D imaging methods with linear or matrix arrays are available in most industrial Non-Destructive Testing (NDT) systems [1,2]. The most popular is the Total Focusing Method (TFM), which requires the inter-element response acquisition often referred to as Full Matrix Capture (FMC) [3]. The set of FMC signals are focused numerically both in transmit and receive mode everywhere in the region of interest, which greatly improves the spatial resolution compared to focused B-scan or S-scan [4]. 2D matrix arrays offer the great advantage of allowing 3D imaging without any displacement [5–7]. However, the 3D TFM remains a challenge for real-time applications due to time-consuming reconstructions. Indeed, the number of signals to be processed is huge as it corresponds to the square of the number of array elements, which is typically equal to 256 in NDT. In addition, the number of points to be reconstructed is generally two orders of magnitude greater than in 2D imaging. The problem is therefore to process this large amount of data in a short period of time. To this end, the Plane Wave Imaging (PWI) method, initially developed for elastography in medical imaging [8], has been adapted to various NDT inspection configurations, such as multi-mode imaging of crack-like defects [9,10] or imaging under complex surfaces [11,12]. In most cases, the transmission of plane waves reduces the amount of data to be processed while maintaining a similar image quality compared to

the TFM. Today the PWI method is already available in some NDT acquisition systems to speed up imaging in 2D [13], but the principle of plane wave emissions remains still insufficient to achieve 3D real-time imaging with current NDT systems.

The TFM and PWI reconstructions take place in the time-domain and are based on the Delay-And-Sum (DAS) principle, where the signals are delayed for each divergent or plane wave emission and then coherently summed. Another way to compute images is to use Fourier-domain algorithms that lead to shorter computation times than the DAS algorithms. The two best-known Fourier-domain imaging methods are the Stolt's migration based on the exploding reflector model [14,15] and the wavenumber algorithm. The second is more suitable in many NDT configurations because it remains valid when images are wider than the array aperture [16,17] or when images of crack type defects involve multi-mode ultrasonic paths [10]. The wavenumber algorithm consists in computing the spectrum of the set of signals on a specific wavenumber grid that depends on the chosen reconstruction region, and then in obtaining the image by inverse Fourier transform. It was first used in Synthetic Aperture Radar (SAR) imaging with a monostatic configuration [18] and later with a bistatic one [19]. In the field of NDT, Hunter et al. [20] propose to extend the method to FMC data in order to reduce computation times in 2D imaging compared to TFM. Almost at the same time, Cheng and Lu [21] proposed a similar

\* Corresponding author.

E-mail address: [maxance.marmonier@gmail.com](mailto:maxance.marmonier@gmail.com) (M. Marmonier).

algorithm dedicated to 2D imaging with plane wave emissions. In NDT, the performances of the Fourier-domain algorithms are generally evaluated in 2D cases [22] where real-time frame rates can be achieved with approaches that are more usual. Here, we propose to study the efficiency of these algorithms for 3D applications where real-time imaging remains a difficult task whatever the method.

In this paper, we present an implementation of both TFM and PWI in 3D as well as their frequency-domain counterparts, referred to as k-TFM and k-PWI in the following. In both cases, the aforementioned frequency-domain algorithms are used in order to increase frame rates. They are compared to the time-domain TFM and PWI in terms of image quality, frame rates and memory requirements. For the k-TFM, the wavenumber algorithm is generalized to 3D imaging with matrix arrays, while for the k-PWI, we follow the same approach as Merabet et al. [16] based on the theory developed by Cheng and Lu [21]. The four imaging algorithms are implemented in a versatile Vantage system allowing to perform acquisitions and reconstructions directly with Matlab (Mathworks). The Matlab parallel computing toolbox is used in order to launch all computations on a graphic card and perform real-time imaging. Finally, the four real-time imaging algorithms are evaluated on an additively manufactured stainless steel sample containing a 3D network of equispaced spherical porosities.

The paper is organized as follows. In Section 2, the theoretical background of 3D imaging is presented. We first recall the mathematical formulation of the time-domain TFM and PWI based on the DAS algorithms, and of their frequency-domain counterparts, i.e. k-TFM and k-PWI. The relationship between the image and the signal spectra is derived for both types of acquisition. In Section 3, some technical details and tricks to improve real-time imaging are provided. In particular, we propose an implementation of the Fourier-domain algorithms that greatly reduces the required memory space. Minimum storage capacity and algorithmic complexities for k-TFM and k-PWI are derived and compared to those obtained with TFM and PWI. In Section 4, we present the experimental setup and the results from the real-time imaging of the steel sample. The image qualities and frame rates are discussed and compared with theoretical and numerical predictions.

## 2. Theoretical background in 3D imaging

In this section, the 3D imaging algorithms are over-viewed. For sake of clarity, we only present the theory for a square matrix array and an inspection configuration where elements are in direct contact with the sample. However, given that inspections through a water layer are quite common in NDT, in Appendix A we derive the method accounting for the refraction at the fluid–solid interface.

### 2.1. Time-domain methods: TFM and PWI

For the FMC, the array elements are excited one by one to transmit  $N$  divergent waves, where  $N$  is the total number of elements. As  $N$  signals are recorded for each transmission, the dataset to handle is composed of  $N^2 N_t$  samples with  $N_t$  the number of time samples. As indicated in Fig. 1(a),  $\mathbf{v} = (v_1, v_2, 0)^T$  and  $\mathbf{u} = (u_1, u_2, 0)^T$  are the vectors that locate respectively the transmitting and receiving element centers. The origin of the Cartesian coordinate system is placed at the center of the matrix and the sets of transmitter and receiver positions are denoted  $\mathcal{V}$  and  $\mathcal{U}$ .

The TFM consists in focusing in transmission and reception at every point in the region of interest. If  $s(\mathbf{u}, \mathbf{v}, t)$  is the signal received by the element at  $\mathbf{u}$  when the element at  $\mathbf{v}$  is excited by an impulse signal, the TFM image is built as the coherent sum of  $N^2$  analytic signals  $\hat{s}(\mathbf{u}, \mathbf{v}, t) = s(\mathbf{u}, \mathbf{v}, t) + j\mathcal{H}\{s(\mathbf{u}, \mathbf{v}, t)\}$  with appropriate time delays [4,23], where  $\mathcal{H}$  denotes the Hilbert transform. Using these notations, the

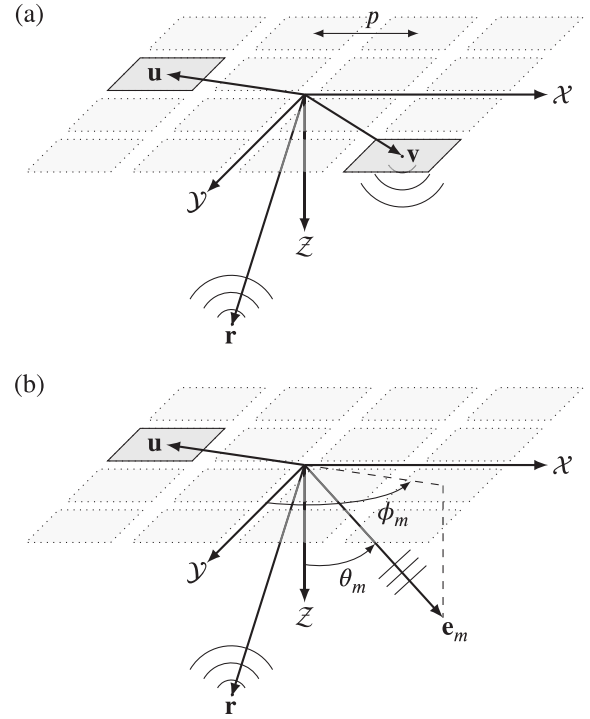


Fig. 1. Geometries and notations used for 3D imaging with divergent or plane waves: (a) transmission of a spherical wave from a single element centered at  $\mathbf{v} = (v_1, v_2, 0)^T$ ; (b) transmission of a plane wavefront of normal vector  $\mathbf{e}_m$  by time delayed excitations of all array elements. For both transmission types, all the receivers of coordinates  $\mathbf{u} = (u_1, u_2, 0)^T$  are used to record  $N$  signals.

image amplitude at a given voxel located by the position vector  $\mathbf{r}$  for a Dirac excitation is defined as

$$I_{\text{TFM}}(\mathbf{r}) = \left| \sum_{\mathbf{u} \in \mathcal{U}} \sum_{\mathbf{v} \in \mathcal{V}} \hat{s} \left( \mathbf{u}, \mathbf{v}, \frac{\|\mathbf{v} - \mathbf{r}\| + \|\mathbf{u} - \mathbf{r}\|}{c} \right) \right|, \quad (1)$$

where  $c$  is the phase velocity of longitudinal or transverse ultrasonic waves depending on the NDT application.

For the PWI method, we assume that the solid is insonified by  $M$  plane waves propagating in different directions. As shown in Fig. 1(b), each plane wave is indexed by  $m$  where  $m \in \mathcal{M} = [1, \dots, M]$  and have a wave vector equal to  $k\mathbf{e}_m$  where

$$\mathbf{e}_m = (\sin \theta_m \cos \phi_m, \sin \theta_m \sin \phi_m, \cos \theta_m)^T, \quad (2)$$

with  $(\theta_m, \phi_m)$  the pair of angles defining the direction of propagation of the  $m$ th plane wave and  $k$  the wavenumber. If all elements are used as receivers, then the number of samples to be stored after  $M$  transmission is  $MN N_t$ . Similarly to the TFM, if  $s_m(\mathbf{u}, t)$  is the signal received by the element at  $\mathbf{u}$  for the  $m$ th emission, the PWI image results from a coherent sum of  $MN$  analytic signals  $\hat{s}_m(\mathbf{u}, t) = s_m(\mathbf{u}, t) + j\mathcal{H}\{s_m(\mathbf{u}, t)\}$  [16]. The image amplitude at a point  $\mathbf{r}$  is defined as

$$I_{\text{PWI}}(\mathbf{r}) = \left| \sum_{\mathbf{u} \in \mathcal{U}} \sum_{m \in \mathcal{M}} \hat{s}_m \left( \mathbf{u}, \frac{\mathbf{r} \cdot \mathbf{e}_m + \|\mathbf{u} - \mathbf{r}\|}{c} + \tau_m \right) \right|, \quad (3)$$

where  $\tau_m$  is the emission delay of one element taken as reference.

In practice, the signals  $s$  and  $s_m$  are known only for times  $t$  in a set of recorded time samples  $\mathcal{T}$ . Thus, the acquisition gate has to be carefully chosen to allow the image computation at all points in the region of interest. Furthermore, in Eqs. (2) and (3),  $\hat{s}$  and  $\hat{s}_m$  must be interpolated to accurately extract the amplitudes corresponding to the theoretical arrival times. A nearest neighbor interpolation is a sufficiently good approximation if the sampling frequency  $f_s$  is large with respect to the central frequency of the array.

## 2.2. Frequency-domain methods: k-TFM and k-PWI

The general idea of the Fourier-domain imaging methods is to use the mathematical relation between the Fourier transform of the dataset and the Fourier transform of the reflector distribution in the medium. Here, the theory of the Fourier-domain imaging is presented in 3D: first k-TFM where spherical waves insonify the medium, then k-PWI with plane wave transmissions. 3D k-TFM is an extension of the work of Hunter et al. [20] to matrix arrays, while 3D k-PWI was recently developed by Merabet et al. [16,17] based on the work of Cheng and Lu [21].

### 2.2.1. 3D k-TFM method

Let us consider a spherical wave transmitted by an element located at  $\mathbf{v}$ , backscattered by a distribution of isotropic point-like reflectors, and received by an element located at  $\mathbf{u}$ . Assuming that there is no attenuation and that the elements have omnidirectional radiation patterns, the time Fourier transform of  $s$  may be written as

$$S(\mathbf{u}, \mathbf{v}, k) = \frac{1}{(4\pi)^2} \int \frac{e^{-ik\|\mathbf{v}-\mathbf{r}\|}}{\|\mathbf{v}-\mathbf{r}\|} g(\mathbf{r}) \frac{e^{-ik\|\mathbf{u}-\mathbf{r}\|}}{\|\mathbf{u}-\mathbf{r}\|} d\mathbf{r}, \quad (4)$$

where  $g$  is the distribution of point-like reflectors and  $d\mathbf{r} = dx dy dz$ . For sake of brevity, the factor in front of the integral in Eq. (4) is omitted in the following. We denote by  $\hat{S}$  the 5-D Fourier transform of  $s$ ,  $\mathbf{k}_r = (k_x, k_y, k_z)^T$ ,  $\mathbf{k}_u = (k_{u_1}, k_{u_2}, 0)^T$  and  $\mathbf{k}_v = (k_{v_1}, k_{v_2}, 0)^T$  the wave vectors corresponding to  $\mathbf{r}$ ,  $\mathbf{u}$  and  $\mathbf{v}$ , respectively. Following the same approach than in 2D [20], we use the Weyl identity to decomposed each Green function in Eq. (4) as continuous sum of plane waves [24], and the 3D Fourier transform of  $g$  can be expressed as

$$\hat{G}(\mathbf{k}_r) = K_u K_v \hat{S}(\mathbf{k}_u, \mathbf{k}_v, k), \quad (5)$$

provided that  $\mathbf{k}_r$ ,  $\mathbf{k}_u$ ,  $\mathbf{k}_v$  and  $k$  satisfy the relation

$$\mathbf{k}_r = \mathbf{K}_u + \mathbf{K}_v \quad (6)$$

where, noting  $w = u$  or  $v$ ,  $\mathbf{K}_w = (k_{w_1}, k_{w_2}, K_w)^T$  and  $K_w = \sqrt{k^2 - k_{w_1}^2 - k_{w_2}^2}$ .

To compute an image, we need to express  $\mathbf{k}_u$ ,  $\mathbf{k}_v$  and  $k$  as a function of  $\mathbf{k}_r$ . As the problem is ill-posed with three equations for five unknowns, we solve it by fixing  $\mathbf{k}_v$  in Eq. (6). The solution is expressed as

$$\begin{cases} k_{u_1} &= & k_x - k_{v_1} \\ k_{u_2} &= & k_y - k_{v_2} \\ k &= & \frac{1}{2k_z} \sqrt{(k_z^2 + \|\mathbf{k}_v\|^2 - \|\mathbf{k}_u\|^2)^2 + 4k_z^2 \|\mathbf{k}_u\|^2} \end{cases}. \quad (7)$$

Thus, we can compute a spectrum  $\hat{G}$  from the spectrum  $\hat{S}$  at a fixed value of  $\mathbf{k}_v$  that will be denoted  $\hat{S}_{\mathbf{k}_v}$  in the following. Then, the spectra are added for all  $\mathbf{k}_v$ , and the final image is obtained by the 3D inverse Fourier Transform over dimensions  $k_{u_1}$ ,  $k_{u_2}$  and  $k$ , noted  $\mathcal{F}_{\mathbf{k}_u, k}^{-1}$ . Finally, the imaging equation is

$$I_{k\text{-TFM}}(\mathbf{r}) = \left| \mathcal{F}_{\mathbf{k}_u, k}^{-1} \left\{ \sum_{\mathbf{k}_v \in \mathcal{K}_v} K_u K_v \hat{S}_{\mathbf{k}_v}(\mathbf{k}_u, k) \right\} \right|, \quad (8)$$

where Eq. (7) provides the required frequencies of the spectra  $\hat{S}_{\mathbf{k}_v}$  and where the set  $\mathcal{K}_v$  is the wavenumber counterpart of  $\mathcal{V}$ .

### 2.2.2. 3D k-PWI method

The imaging equation for k-PWI is derived in the same way as previously. First, we express the time Fourier transform of  $s_m$  as

$$S_m(\mathbf{u}, k) = \frac{1}{4\pi} \int e^{-ik\mathbf{r} \cdot \mathbf{e}_m} g(\mathbf{r}) \frac{e^{-ik\|\mathbf{u}-\mathbf{r}\|}}{\|\mathbf{u}-\mathbf{r}\|} d\mathbf{r}, \quad (9)$$

Here, the Weyl identity needs to be used only once to replace the Green function in Eq. (9), which leads to

$$\hat{G}(\mathbf{k}_r) = K_u \hat{S}_m(\mathbf{k}_u, k), \quad (10)$$

with  $\hat{S}_m$  the 3D Fourier transform of  $s_m$  and where  $\mathbf{k}_r$ ,  $\mathbf{k}_u$  and  $k$  must satisfy the relation

$$\mathbf{k}_r = \mathbf{K}_u + k\mathbf{e}_m. \quad (11)$$

From Eq. (11),  $\mathbf{k}_u$  and  $k$  can be expressed as a function of  $\mathbf{k}_r$ . We obtain

$$\begin{cases} k_{u_1} &= & k_x - k \sin \theta_m \cos \phi_m \\ k_{u_2} &= & k_y - k \sin \theta_m \sin \phi_m \\ k &= & \frac{\|\mathbf{k}_r\|^2}{2\mathbf{k}_r \cdot \mathbf{e}_m} \end{cases}. \quad (12)$$

Thus, a spectrum  $\hat{G}$  is calculated for each incident plane wave. The spectra corresponding to  $M$  plane waves are added and the final image is obtained by 3D inverse Fourier transform. The imaging equation is

$$I_{k\text{-PWI}}(\mathbf{r}) = \left| \mathcal{F}_{\mathbf{k}_u, k}^{-1} \left\{ \sum_{m \in \mathcal{M}} K_u \hat{S}_m(\mathbf{k}_u, k) \right\} \right|, \quad (13)$$

where Eq. (12) provides the required frequencies of the spectra  $\hat{S}_m$ .

## 3. Implementation of imaging algorithms

In this section, the implementation of the time-domain and Fourier-domain methods is presented in detail. First, the strategy adopted to compute the signal spectra is described. In particular, we propose a method to compute the signal spectra without resorting to any interpolation along the two lateral spatial dimensions. Then, the imaging algorithms in the time and frequency domains are compared in terms of required memory space and complexities.

### 3.1. Computation of the signal spectra

The frequencies  $(\mathbf{k}_u, k)$  required for k-TFM and k-PWI depend on the desired image frequencies  $\mathbf{k}_r$  and are defined by Eqs. (7) and (12). However, in practice, the spectra  $\hat{S}_{\mathbf{k}_v}$  and  $\hat{S}_m$  are computed with Discrete Fourier Transforms (DFTs) on the wavenumber grid  $\mathcal{K}_U \times \mathcal{K}_T$  given by

$$\begin{cases} \mathcal{K}_U &= & \left[ -\frac{N_{k_{u_1}}}{2} + 1, \dots, \frac{N_{k_{u_1}}}{2} \right] \frac{2\pi}{N_{k_{u_1}} p} \\ &\times & \left[ -\frac{N_{k_{u_2}}}{2} + 1, \dots, \frac{N_{k_{u_2}}}{2} \right] \frac{2\pi}{N_{k_{u_2}} p} \times \{0\}, \\ \mathcal{K}_T &= & \left[ -\frac{N_k}{2} + 1, \dots, \frac{N_k}{2} \right] \frac{2\pi f_s}{N_k c} \end{cases}, \quad (14)$$

where  $p$  is the pitch of the matrix array and  $N_{k_{u_1}}$ ,  $N_{k_{u_2}}$  and  $N_k$  are respectively the lengths of the Fourier transforms along the dimensions  $k_{u_1}$ ,  $k_{u_2}$  and  $k$ . Provided that DFTs are computed without zero-padding,  $N_{k_{u_1}}$  and  $N_{k_{u_2}}$  are equal to  $\sqrt{N}$  and  $N_k$  to the number of time samples  $N_t$ . The problem is to obtain the spectra on the required wavenumber grid instead, and a classical way to do this is to interpolate the initial spectra known on  $\mathcal{K}_U \times \mathcal{K}_T$ . In this paper, only the dimension  $k$  will be treated in this way, while a method is proposed to compute the signal spectra without any interpolation along the lateral dimensions  $k_{u_1}$  and  $k_{u_2}$ .

In this method, the shifted signal spectra  $\hat{S}'_{\mathbf{k}_v}$  and  $\hat{S}'_m$  are used instead of the original signal spectra  $\hat{S}_{\mathbf{k}_v}$  and  $\hat{S}_m$ . These spectra are calculated applying a phase shift before the spatial Fourier transform, which is written as

$$\hat{S}'_{\mathbf{k}_v}(\mathbf{k}_u, k) = \mathcal{F}_u \left\{ S_{\mathbf{k}_v}(\mathbf{u}, k) e^{i\mathbf{k}_v \cdot \mathbf{u}} \right\} \quad (15)$$

and

$$\hat{S}'_m(\mathbf{k}_u, k) = \mathcal{F}_u \left\{ S_m(\mathbf{u}, k) e^{i\mathbf{k}'_m \cdot \mathbf{u}} \right\}, \quad (16)$$

where  $\mathcal{F}_u$  is the Fourier transform along the dimensions  $u_1$  and  $u_2$ . If  $\hat{S}_{\mathbf{k}_v}$  and  $\hat{S}_m$  are replaced respectively by  $\hat{S}'_{\mathbf{k}_v}$  and  $\hat{S}'_m$ , the expressions

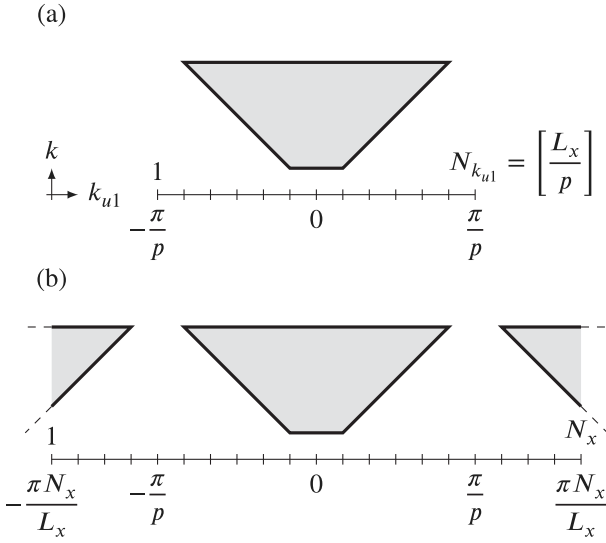


Fig. 2. Diagram of spectral extension principle for an image of length  $L_x$  along the  $x$  axis: (a) initial spectrum ; (b) spectrum after extension. The trapezoidal area in gray represents the support of propagative waves.

of the required wavenumbers  $k_{u_1}$  and  $k_{u_2}$  in Eqs. (7) and (12) simplify and become  $k_{u_1} = k_x$  and  $k_{u_2} = k_y$ . Satisfying these two relations means having equality between the first two dimensions of  $\mathcal{K}_V$  and the desired lateral grid  $\mathcal{K}_x \times \mathcal{K}_y$ , where

$$\begin{cases} \mathcal{K}_x &= \left[ -\frac{N_x}{2} + 1, \dots, \frac{N_x}{2} \right] \frac{2\pi}{L_x} \\ \mathcal{K}_y &= \left[ -\frac{N_y}{2} + 1, \dots, \frac{N_y}{2} \right] \frac{2\pi}{L_y} \end{cases} \quad (17)$$

In other words, it is necessary to have equal sampling steps as well as equal number of points for  $\mathcal{K}_x \times \mathcal{K}_y$  and the first two dimensions of  $\mathcal{K}_V$ . To this end, the method comprises two steps.

The first is zero-padded Fourier transform along the  $u_1$  and  $u_2$  dimensions of the above shifted signal spectra  $S'_{k_v}$  and  $S'_m$ . The number of points  $N_{k_{u_1}}$  and  $N_{k_{u_2}}$  are chosen so that the wavenumber pitch is identical for the dimensions  $k_{u_1}$  and  $k_x$  as well as for the dimensions  $k_{u_2}$  and  $k_y$ . For a volume with lateral sizes  $L_x$  and  $L_y$ , the wavenumber sampling step along the dimensions  $k_x$  and  $k_y$  must be equal to  $2\pi/L_x$  and  $2\pi/L_y$ . Furthermore, the pitch  $p$  of the matrix probe along the  $x$  and  $y$  axes imposes that the computed spectra vary between  $-\pi/p$  and  $\pi/p$ . Thus, we choose

$$N_{k_{u_1}} = \left\lceil \frac{L_x}{p} \right\rceil \quad (18)$$

and

$$N_{k_{u_2}} = \left\lceil \frac{L_y}{p} \right\rceil. \quad (19)$$

The second step is to extend the obtained discrete spectra. For a given spectrum known between  $-\pi/p$  and  $\pi/p$ , an extension by periodicity over any interval is possible, as illustrated in Fig. 2 for the dimension  $k_{u_1}$ . The lower and upper bounds of the wavenumber grid are chosen equal to  $-\pi N_x/L_x$  and  $\pi N_x/L_x$  for the dimension  $k_{u_1}$  and equal to  $-\pi N_y/L_y$  and  $\pi N_y/L_y$  for the dimension  $k_{u_2}$ . In this way, the amplitudes of the spectra  $\hat{S}'_{k_v}$  and  $\hat{S}'_m$  are directly obtained on the desired wavenumber grid  $\mathcal{K}_x \times \mathcal{K}_y$ , without any interpolation. Note that we do not directly apply an inverse DFT to this extended spectrum, it is only used for the interpolation step. This makes it possible to obtain an image spectrum after interpolation having a wider support than if zeros were added instead of extending the signal spectra, which improves the quality of the reconstructed images.

The expression of  $k$  in Eqs. (7) and (12) is non-linear with respect to  $k$ , and so, the required wavenumber grid for  $k$  is non-uniform. Thus, the method described above is not applicable for this dimension and, as previously mentioned, an interpolation of the signal spectra along the  $k$  dimension is performed. A nearest neighbor interpolation is chosen but, knowing that the interpolation accuracy is a preponderant factor for the quality of the Fourier-domain reconstructions, zero-padding is used for the time dimension before DFT computation and  $N_k$  is chosen large enough to obtain a satisfactory image quality. Note that different ways are proposed in the literature. For example, by improving the quality of the interpolation step [25], by using a non-uniform FFT [26,27] or by using the interpolation-free Stolt mapping method developed by Li et al. [28]. However, the amount of memory required for these algorithms will be greater and the obtained frame rate lower. For real-time 3D imaging, the use of zero-padding and nearest neighbor interpolation seems to be a good compromise to obtain good performance without excessively degrading the image quality.

### 3.2. Required memory space

Regarding the real-time implementation of imaging algorithms, high frame rates can be reached if all matrices needed to reconstruct an image are computed before starting the imaging loop. However, large enough memory space is required to store the reconstruction algorithm matrices, in addition to the recorded signals. This is the main constraint for real-time imaging. In this paper, we do not make a trade-off between frame rates and memory requirements and we only present the fastest possible implementation and therefore the most memory intensive.

For TFM and PWI, the computation of  $N \times N$  and  $N \times M$  arrival times is needed for each reconstruction point in the region of interest. For each of these times, the index of the closest value in  $\mathcal{T}$  is stored in the graphic card. In the same way, for the Fourier-domain algorithms, the indices corresponding to the closest values in  $\mathcal{K}_T$  of the required values of  $k$  are stored in the memory space of the graphic card. Using shifted signal spectra reduces the number of indexes to be stored by a factor of  $N$  for the k-TFM and k-PWI methods because the required  $k$  in Eqs. (7) and (12) no longer depend on  $k_{u_1}$  and  $k_{u_2}$  which are imposed equal to  $k_x$  and  $k_y$  in this case. The skew factors  $K_u$  and  $K_v$ , as well as the phase shifts in Eqs. (15) and (16) and those used for taking into account a water/solid interface (see Appendix A), are also computed and stored.

The sizes of the different stored matrices are summarized in Table 1 and the memory requirements corresponding to our experimental settings are presented in Fig. 3(a). It appears that our implementation of the Fourier-domain algorithms provides lower memory costs compared to those in the time domain. This is especially valuable in the context of 3D real-time imaging where the amount of available memory in NDT systems is a huge constraint if large volumes have to be reconstructed with high resolutions. In our experiment, where  $N = 256$ ,  $M = 33$ ,  $N_t = 237$ ,  $N_k = 711$ ,  $L_x = 9.9$  mm,  $L_y = 9.9$  mm and  $N_x = N_y = N_z/2$ , k-TFM requires approximately 80 times less memory space than TFM for  $10^5 < N_{xyz} < 10^8$  where  $N_{xyz} = N_x N_y N_z$  is the total number of voxels. In the case of plane wave emission and for the same range of  $N_{xyz}$  values, k-PWI has memory requirement between 2 and 60 times lower than PWI.

### 3.3. Algorithmic complexity analysis

For the TFM and PWI methods, the signal amplitudes in the dataset are extracted using the indices stored in the graphic card. This operation is a nearest neighbor interpolation of the signals that comprises only memory accesses. The results of the interpolation step are stored in a 5-D double array of size  $N_x \times N_y \times N_z \times N \times N$  for the TFM method and  $N_x \times N_y \times N_z \times N \times M$  for the PWI method. Each component of those 5-D variable corresponds to an amplitude extracted in the

**Table 1**  
Types and sizes of the variables precomputed and stored in the graphic card.

Variable	Type	Size			
		TFM	k-TFM	PWI	k-PWI
Interpolation indices	uint32	$N_x N_y N_z N^2$	$N_x N_y N_z N$	$N_x N_y N_z N M$	$N_x N_y N_z M$
Skew factors	single complex		$N_x N_y N_z N$		$N_x N_y N_z M$
Signals phase shift	single complex		$N^2$		$N_k N M / 2$
Water phase shift	single complex		$N_k N_x N_y N / 2$		$N_k N_x N_y M / 2$

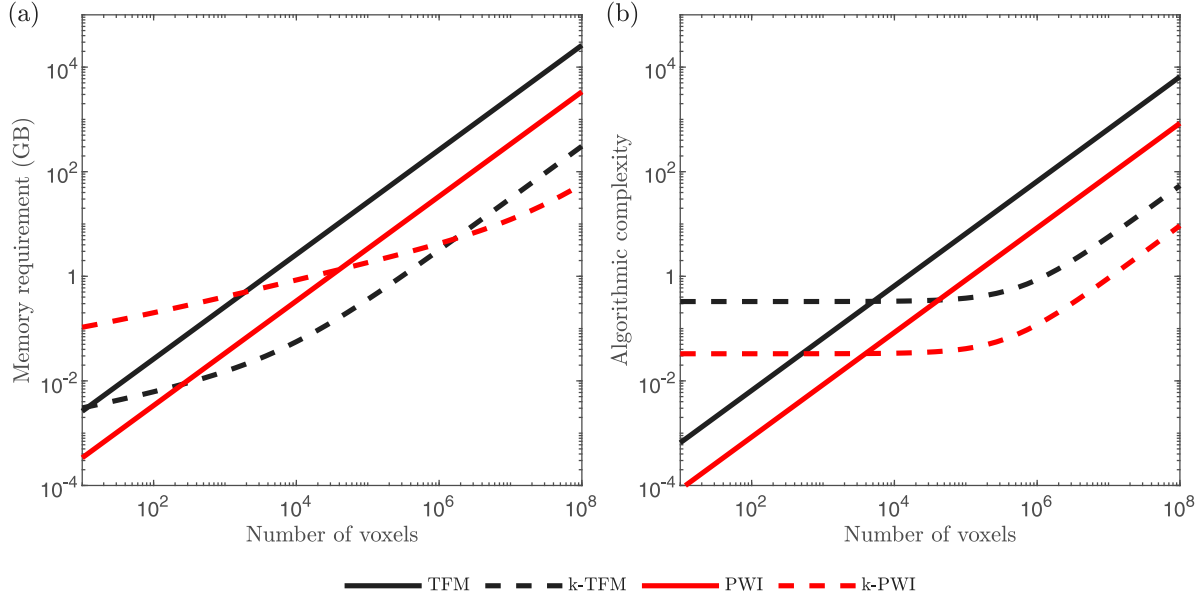


**Fig. 3.** Required memory (a) and algorithmic complexity (b) plotted as a function of the number of voxels for TFM, PWI, k-TFM and k-PWI. The results correspond to the acquisition and reconstruction parameters used in the experiments:  $N = 256$ ,  $M = 33$ ,  $N_t = 237$ ,  $N_k = 711$ ,  $L_x = 9.9$  mm,  $L_y = 9.9$  mm and  $N_x = N_y = N_z/2$ .

experimental dataset at a corresponding arrival time. For both methods, the calculation of a single voxel requires a double summation (see Eqs. (1) and (3)). Thus, for  $N_{xyz}$  voxels, the algorithmic complexities for TFM and PWI are respectively

$$C_{\text{TFM}} = N_{xyz} N^2 \quad (20)$$

and

$$C_{\text{PWI}} = N_{xyz} M N. \quad (21)$$

For the k-TFM algorithm, the 5-D Fourier transform of the dataset must be computed before interpolation. As explained before, zero-padding is used for the DFT computations along the dimensions  $u_1$ ,  $u_2$  and  $t$  with the number of points  $N_{k_{u_1}}$ ,  $N_{k_{u_2}}$  and  $N_k$ . Thus, this 5-D Fourier transform comprises the following computation steps:

1. Zero-padded DFT along the time dimension with suppression of the useless negative frequencies;
2. DFTs along the dimensions  $v_1$  and  $v_2$ ;
3. Application of phase shifts before zero-padded DFTs along the dimensions  $u_1$  and  $u_2$ .

Direct and inverse DFTs are computed using the Fast Fourier Transform (FFT) and the algorithmic complexity of the 5-D FFT is therefore equal to  $N_k N_{k_{u_1}} N_{k_{u_2}} N \log_2 \left( N_k \sqrt{N_{k_{u_1}} N_{k_{u_2}} N} \right)$ . The application of the phase shift corresponds to a term-by-term multiplication of two 5-D arrays of size  $\frac{N_k}{2} \times \sqrt{N} \times \sqrt{N} \times \sqrt{N} \times \sqrt{N}$  which has therefore an algorithmic complexity equal to  $\frac{N_k}{2} N^2$ . After the extension of the spectrum along the dimensions  $k_{u_1}$  and  $k_{u_2}$ , a nearest neighbor interpolation is performed along the dimension  $k$ . We thus obtain a 5-D array of size  $N_x \times N_y \times N_z \times \sqrt{N} \times \sqrt{N}$  that we multiply by  $K_u K_v$  and sum over the two last dimensions. Each of these two operations has a complexity

equal to  $N_{xyz} N$  and finally, an image spectrum is stored in a 3D array of size  $N_x \times N_y \times N_z$ . The last operation is an inverse 3D FFT with complexity equal to  $N_{xyz} \log_2(N_{xyz})$ . All these above operations lead to an algorithmic complexity for k-TFM equal to

$$C_{\text{k-TFM}} = N_k N_{k_{u_1}} N_{k_{u_2}} N \log_2 \left( N_k \sqrt{N_{k_{u_1}} N_{k_{u_2}} N} \right) + \frac{N_k}{2} N^2 + 2N_{xyz} N + N_{xyz} \log_2(N_{xyz}). \quad (22)$$

k-PWI includes the same computation steps, which leads to a similar algorithmic complexity:

$$C_{\text{k-PWI}} = N_k N_{k_{u_1}} N_{k_{u_2}} M \log_2 \left( N_k \sqrt{N_{k_{u_1}} N_{k_{u_2}} N} \right) + \frac{N_k}{2} N M + 2N_{xyz} M + N_{xyz} \log_2(N_{xyz}). \quad (23)$$

In this expression, the first term corresponds to the calculation of  $M$  3D FFT, one for each transmission. It is the main difference with the algorithmic complexity expression of k-TFM where the first term corresponds to a single 5-D FFT of the entire recorded data set. The other differences are simply due to the different numbers of transmissions for both methods. Each algorithmic complexity consists in two mains contributions: the first corresponds to the Fourier transform of the dataset and mainly depends on the number  $N$  of array elements; and the second corresponds to the inverse Fourier transform of the image spectrum and mainly depends on the number of voxels  $N_{xyz}$ .

The algorithmic complexities of the four imaging methods were estimated considering the matrix probe and the imaging parameters used in our experiment, and are plotted as a function of the number of voxels in Fig. 3(b). Using the Fourier-domain algorithms leads to lower algorithmic complexities, but only for a number of reconstructed voxels greater than  $5 \cdot 10^3$  in our configuration. As the desired number

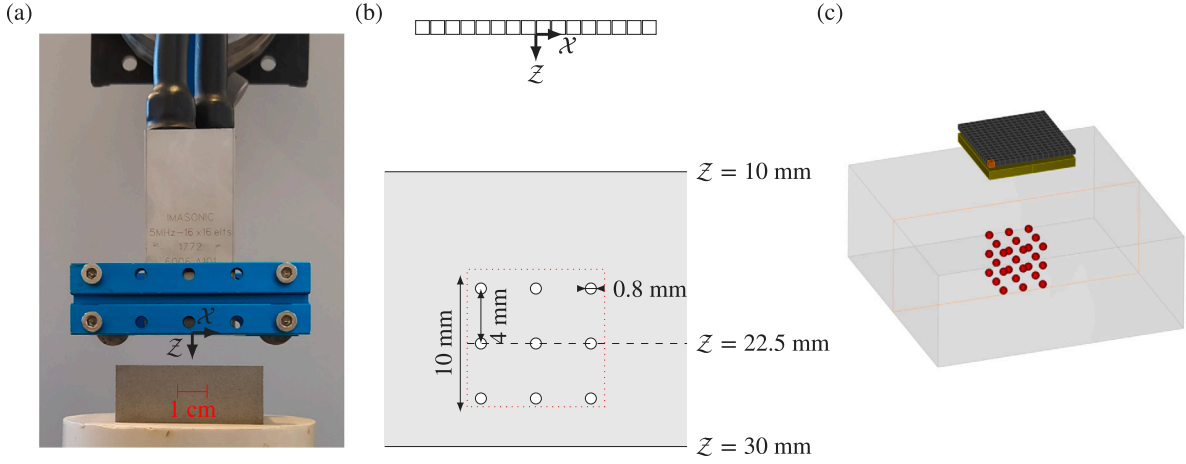


**Fig. 4.** Experimental setup with a matrix array and a stainless steel block immersed in water (a). The block was elaborated by additive manufacturing and contains 27 porosities of 0.8 mm diameter arranged in a 3D network of 4 mm period: side view with a water column height of 10 mm (b); 3D view (c).

of voxels in 3D imaging typically varies between  $10^5$  and  $10^8$ , the Fourier-domain algorithms are therefore useful to speed up real-time 3D imaging. However, if a matrix array with more elements is used, the imaging algorithms will be more efficient in the time domain rather than in the frequency domain for a larger range of number of voxels. Indeed, the terms that mainly depend of the number of elements in the algorithmic complexities of the Fourier-domain methods will stay preponderant for a larger number of reconstruction points.

An analysis of (22) and (23) shows that the gains in terms of numbers of operations for the Fourier-domain algorithms for  $10^5 < N_{xyz} < 10^8$  are given by

$$\frac{C_{k\text{-TFM}}}{C_{\text{TFM}}} \sim \frac{2N + \log_2(N_{xyz})}{N^2} \quad (24)$$

and

$$\frac{C_{k\text{-PWI}}}{C_{\text{PWI}}} \sim \frac{2M + \log_2(N_{xyz})}{NM}. \quad (25)$$

For example, these expressions lead to approximatively 125 times less operations for k-TFM over TFM and of approximatively 95 for k-PWI over PWI. Although this does not directly give us the gain in terms of improved frame rate, it indicates that Fourier domain algorithms are a good tool for performing real-time imaging.

#### 4. Real-time 3D imaging results

In the present section, an additively manufactured 316L stainless steel block containing a set of spherical porosities is imaged with the four imaging methods. First, the experimental setup and the manufacturing additive sample are presented. Then, the quality of the 3D images is compared for a certain number of voxels allowing image computation with the four methods. Finally, the imaging rates for each method as a function of the number of voxels are compared.

##### 4.1. Experimental setup

The experimental setup is shown in Fig. 4. The matrix array manufactured and distributed by Imasonic (Voray-sur-l'Ognon, France) is composed of  $16 \times 16$  square elements of  $1 \text{ mm}^2$  arranged with a pitch of 1.1 mm in the  $\mathcal{X}$  and  $\mathcal{Y}$  directions. The elements operate at the central frequency of 5 MHz. The sample to be imaged is a 316L stainless steel block elaborated by additive manufacturing with a laser powder-bed fusion process. The block includes a network of 27 porosities of 0.8 mm diameter organized in a cubic mesh of 4 mm period with a maximum angle between the reflectors and the probe axis of about  $18^\circ$ . The block

is 20-mm high and is assumed to be isotropic with longitudinal wave velocity equal to  $5.74 \text{ mm } \mu\text{s}^{-1}$  [29]. The experiment was carried out in a water tank and the matrix array placed 10 mm above the sample surface so that its central axis coincides with the central porosities of the 3D network. It should be pointed out that the printed sample was controlled by X-ray radiography to ensure that all the defects are identical spheres and that they are not completely filled with steel powder.

The data acquisition with divergent or plane waves were performed using a 256-channel Vantage (Verasonics) system and the 3D imaging codes were implemented on Matlab 2021a and were launch on a graphic card (Nvidia Geforce RTX 3090) with 24 GB of available memory. The recorded time window is set between 16.25 and 20.05  $\mu\text{s}$ , so the echoes from the specimen surfaces are not digitized. This avoids imaging artifacts possibly caused by aliasing for the Fourier-domain methods [20]. The Vantage system has a programmable sample rate of up to 62.5 MHz. The maximum available sample rate is used, so each recorded signal contains 237 time samples.

For the PWI and k-PWI methods, a satisfactory quality image of the printed sample can be obtained with only 33 plane waves provided that the transmission angles  $(\theta_m, \phi_m)$  are defined as

$$(\theta_m, \phi_m) = \begin{cases} (0, 0) \\ (2.5i, 45j) \end{cases} \text{ where } \begin{cases} i \in [1, \dots, 4] \\ j \in [0, \dots, 7] \end{cases}. \quad (26)$$

It should be noted that our objective is not to obtain the best possible image by increasing the number of plane waves, but to evaluate the benefit of a reconstruction in the Fourier domain for a given number of plane waves. Note also that no apodization was applied at the time of acquisition in order to maintain a satisfactory spatial resolution.

##### 4.2. Comparison of obtained image quality

The 3D images corresponding to TFM, k-TFM, PWI and k-PWI are displayed in Fig. 5 in the form of isosurfaces. The region of interest is a  $10 \text{ mm}^3$  cubic volume centered on the porosity of coordinates  $(0, 0, 22.1)$  located at the center of the 3D network. For each volume, different isovalues are used depending on the depth of the porosities so that all the echoes remain visible with similar sizes. The number of voxels is  $N_x \times N_y \times N_z = 24 \times 24 \times 50$ . This corresponds to voxels of size  $\lambda/3$  in the lateral directions and to  $\lambda/6$  in the axial direction, which is below the resolution limit given by the Rayleigh criterion [30,31]. Furthermore, it corresponds to the maximum number of voxels for which we can reconstruct an image with the four methods due to the limited memory available on the graphics card. Note that the most memory-intensive method is TFM imaging, so it is this method that limits this number.

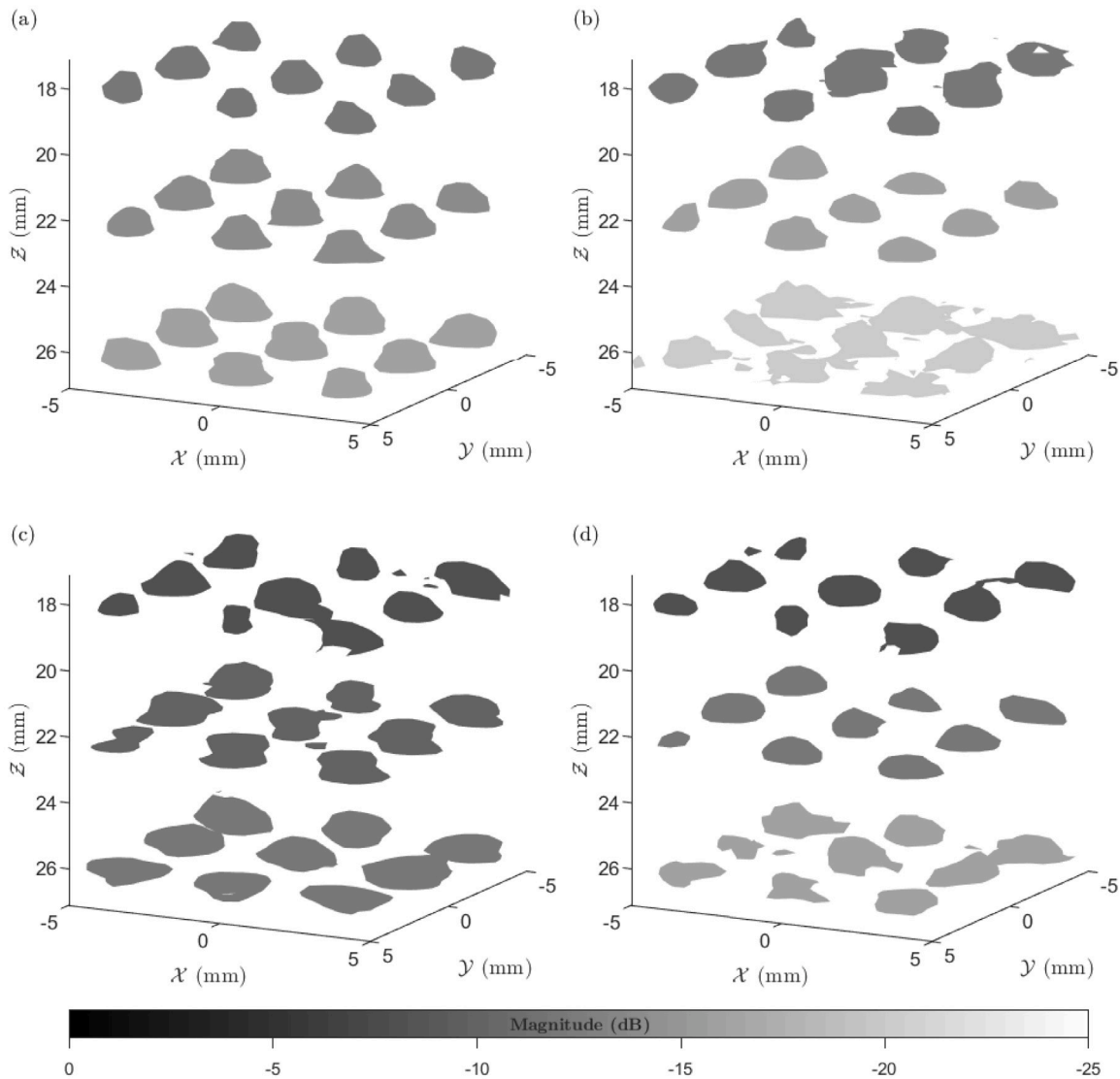


Fig. 5. Experimental 3D images of the network of 27 spherical porosities shown in the form of isosurfaces: (a) TFM; (b) k-TFM; (c) PWI; (d) k-PWI. The 0 dB reference level corresponds to the maximum over amplitude measured in the whole volume, and the isovalues chosen to display the three horizontal networks of 9 porosities are indicated in dB in the table below. (a) TFM. (b) k-TFM. (c) PWI. (d) k-PWI.

A first observation is that all porosities are properly imaged. The different isovalues used suggest that the reconstructed porosity amplitudes decrease faster as a function of the distance from the array for both Fourier-domain reconstructions. For a quantitative comparison, the amplitudes along the vertical central axis of the matrix are plotted in Fig. 6. The amplitude gaps between the top porosity at  $z = 20$  mm and the bottom porosity at  $z = 28$  mm are 7.9 dB for TFM and 13 dB for k-TFM. For PWI and k-PWI, the amplitude gaps correspond to 5.4 and 11.5 dB, respectively. As expected, the amplitudes decrease more rapidly for TFM and k-TFM compared to PWI and k-PWI due to the attenuation by spherical spreading. We also observe that the three highest peaks correctly locate the porosities for all four methods. Indeed, the positioning errors are below the wavelength (1.1 mm) for all the porosities.

The horizontal cross sections are displayed in Fig. 7 for depths  $z = 18.1$  mm,  $z = 22.1$  mm and  $z = 26.1$  mm where the image amplitude

is maximum. They correspond to the top of the spherical defects. For the Fourier-domain methods, we observe that the spatial resolution of the upper plane is better and the image quality degrades more rapidly with depth than the time-domain methods. This is particularly clear for k-TFM. In order to compare the quality of the reconstructions, two metrics are used: the Signal-to-Noise Ratio (SNR) and the Array Performance Indicator (API) [32]. The SNR measures the detectability of a defect in the presence of noise and can be expressed as

$$\text{SNR} = \frac{A_{\text{echo}}}{\sigma_{\text{noise}}}, \quad (27)$$

where  $A_{\text{echo}}$  is the maximum amplitude of a defect echo and  $\sigma_{\text{noise}}$  is the standard deviation of the noise at the same depth. In our experiment,  $\sigma_{\text{noise}}$  was measured by moving the probe over a defect-free region. The API is introduced to quantify the spatial resolution of an imaging

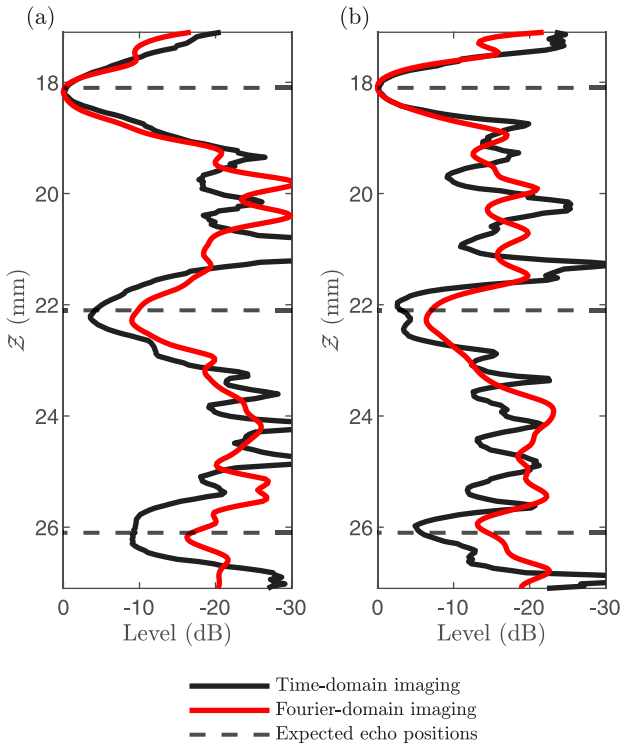


Fig. 6. Amplitudes of the 3D images extracted along the vertical central axis of the matrix array: (a) TFM and k-TFM; (b) PWI and k-PWI.

method and can be expressed as

$$\text{API} = \frac{N_{-6\text{dB}} D_x D_y D_z}{\lambda^3}, \quad (28)$$

where  $D_x$ ,  $D_y$  and  $D_z$  are the dimensions of the voxels along the  $\mathcal{X}$ ,  $\mathcal{Y}$  and  $\mathcal{Z}$  axes, and  $N_{-6\text{dB}}$  is the number of voxels with amplitudes greater than the  $-6$  dB threshold where  $0$  dB corresponds to the maximum reconstructed amplitude of the defect. The SNR and API values measured around the positions of the central porosities are presented in Table 2. The Fourier-domain imaging results in lower SNR values compared to the time-domain reconstructions, and this SNR decay with depth is similar for the TFM and PWI methods. For the upper porosity, Fourier-domain and time-domain imaging provide similar API. However, the API degrades more rapidly with depth for the Fourier-domain imaging.

Following the approach taken by Velichko et al. [33] and Merabet et al. [16], the differences observed experimentally between the 3D images computed in the time and frequency domains can be justified theoretically using asymptotic expansions of the integral expressions of the reflector distributions. The analytical demonstration leading to the imaging equations is summarized in Appendix B. In the simplified case where the array elements are directly in contact with the sample, the imaging equations for TFM and k-TFM can be put into the following integral forms:

$$g_{\text{TFM}}(\mathbf{r}) = \iiint G_{\text{TFM}}(\mathbf{r}, \mathbf{u}, \mathbf{v}, k) d\mathbf{u}d\mathbf{v}dk \quad (29)$$

and

$$g_{\text{k-TFM}}(\mathbf{r}) \underset{kz \rightarrow \infty}{\sim} A^2 \iiint \frac{k^4 \cos^2 \beta(\mathbf{r}, \mathbf{u}) \cos^2 \beta(\mathbf{r}, \mathbf{v})}{\|\mathbf{r} - \mathbf{u}\| \|\mathbf{r} - \mathbf{v}\|} G_{\text{TFM}}(\mathbf{r}, \mathbf{u}, \mathbf{v}, k) d\mathbf{u}d\mathbf{v}dk, \quad (30)$$

where  $G_{\text{TFM}}(\mathbf{r}, \mathbf{u}, \mathbf{v}, k) = S(\mathbf{u}, \mathbf{v}, k) e^{ik(\|\mathbf{r}-\mathbf{v}\| + \|\mathbf{r}-\mathbf{u}\|)}$ ,  $A$  is a complex constant and, noting  $\mathbf{w} = \mathbf{u}$  or  $\mathbf{v}$ ,  $\beta(\mathbf{r}, \mathbf{w})$  is the angle at which a point located at  $\mathbf{r}$  is seen from the element positioned at  $\mathbf{w}$ . For the PWI method, the

Table 2

SNR and API values measured around the positions of the central porosities at  $Z = 18.1$  mm,  $Z = 22.1$  mm and  $Z = 26.1$  mm.

Depth (mm)	SNR (dB)				API			
	TFM	k-TFM	PWI	k-PWI	TFM	k-TFM	PWI	k-PWI
18.1	39	33	16	11	0.43	0.53	0.81	0.7
22.1	41	33	15	8	0.48	0.86	1.2	1.34
26.1	35	28	18	9	1.2	1.9	1.3	2.1

expressions obtained for a single plane wave emission are

$$g_{\text{PWI}}(\mathbf{r}) = \iint G_{\text{PWI}}(\mathbf{r}, \mathbf{u}, k) d\mathbf{u}dk \quad (31)$$

and

$$g_{\text{k-PWI}}(\mathbf{r}) \underset{kz \rightarrow \infty}{\sim} A \iint \frac{k^2 \cos^2 \beta(\mathbf{r}, \mathbf{u})}{\|\mathbf{r} - \mathbf{u}\|} G_{\text{PWI}}(\mathbf{r}, \mathbf{u}, v, k) d\mathbf{u}dk, \quad (32)$$

where  $G_{\text{PWI}}(\mathbf{r}, \mathbf{u}, k) = S_m(\mathbf{u}, k) e^{ik(\mathbf{r} \cdot \mathbf{e}_m + \|\mathbf{r}-\mathbf{u}\|)}$ . For the frequency-domain methods k-TFM and k-PWI, the terms  $G_{\text{TFM}}(\mathbf{r}, \mathbf{u}, \mathbf{v}, k)$  and  $G_{\text{PWI}}(\mathbf{r}, \mathbf{u}, k)$  are multiplied by a function that acts as a space-time filter. The effects of this filters can be summarized in three points:

1. The factors  $\|\mathbf{r} - \mathbf{w}\|^{-1}$  theoretically confirm that the echo amplitudes decrease faster with the distance to the array when images are computed in the frequency domain;
2. The factors  $\beta(\mathbf{r}, \mathbf{w})$  show that the Fourier-domain imaging penalizes the detection of defects located outside of the matrix aperture;
3. The factors in the form of powers of  $k$  shift the spectral content towards the higher frequencies, which improves the resolution of images in the Fourier domain but can also increase the noise sensitivity.

For the first point, the experimental observations are in perfect agreement with the theory since the porosity echoes in the k-TFM and k-PWI images decrease more rapidly with depth compared to what is observed in the TFM and PWI images. As the porosities are all located below the matrix aperture, we cannot make a comparison in relation to the second point. Concerning the third point, our previous study in 3D imaging with simulated echoes confirmed that a better spatial resolution is obtained for the reconstructed images in the Fourier domain in the absence of noise [16]. Looking at the API values, it seems that the greater noise sensitivity of these methods does not allow to find the same results with the experimental data except for the highest central porosity where the k-PWI obtains a better API than the PWI. Furthermore, in the presence of experimental noise, the SNR measured with the Fourier-domain algorithms is lower than that obtained with the time-domain methods. However, in the case of electronic noise, the SNR could be improved by averaging several images since the frame rates are significantly higher for the frequency-domain methods. Provided acquisition time is small compared to image computation time, it should be also possible to increase the SNR by averaging the acquired signals. This is the case when the number of emissions is reduced by using plane wave emissions, for example, and when the region of interest is close to the probe, which allows for a short signal digitization time. Reducing noise in the data in this way is particularly useful for k-TFM and k-PWI as they are more sensitive to noise than TFM and PWI methods, respectively.

#### 4.3. Comparison of obtained frame rates

The frame rates obtained with the four real-time imaging methods are given in Table 3 for voxel numbers ranging from  $3.5 \times 10^3$  to  $1.3 \times 10^7$ . Due to the limited available memory in the graphic card, some algorithms cannot be applied to the larger number of voxels.

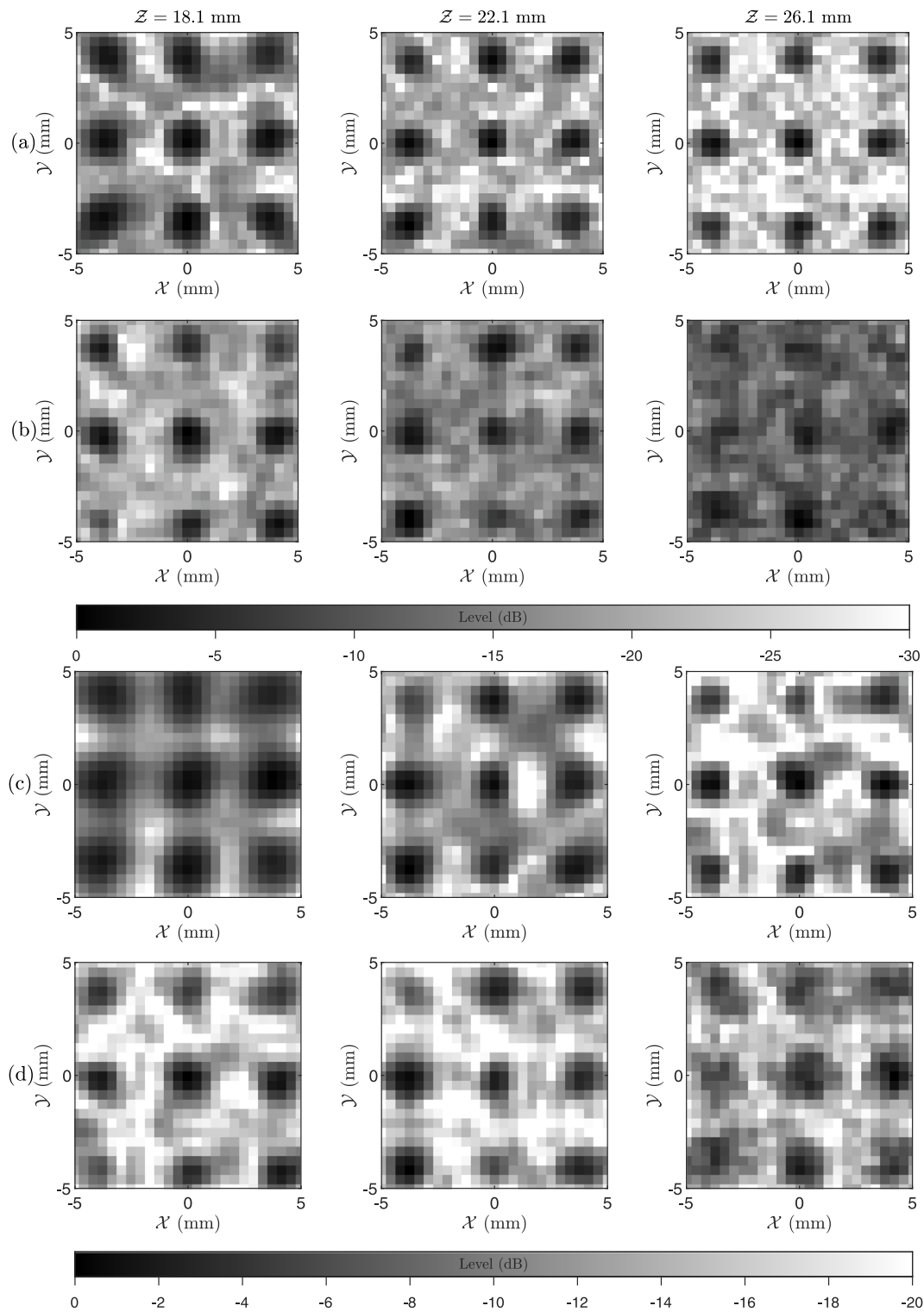


Fig. 7. Horizontal cross sections of reconstructed volumes at  $Z = 18.1$  mm,  $Z = 22.1$  mm and  $Z = 26.1$  mm. (a) TFM. (b) k-TFM. (c) PWI. (d) k-PWI. Level limits are adapted to noise and therefore TFM images are displayed between 0 and  $-30$  dB and PWI ones between 0 and  $-20$  dB.

Our implementation of the algorithms in the Fourier domain allows us to gain a factor 46 on the maximum number of voxels for the TFM and a factor 59 for the PWI. Furthermore, as expected from the analysis of algorithmic complexities, better frame rates are obtained with the Fourier-domain imaging beyond a certain number of voxels, approximately  $10^4$  voxels for the k-TFM method and  $10^5$  voxels for the k-PWI method. For  $24 \times 24 \times 48$  voxels, a TFM image is computed in

333 ms whereas a k-TFM image is computed in 77 ms, i.e. about 4 times faster. In addition, for  $48 \times 48 \times 96$  voxels, a PWI image is computed in 167 ms whereas a k-PWI image is computed in 15 ms, i.e. about 11 times faster. The larger the number of voxels, the more useful the Fourier-domain algorithms. Thus, a low memory cost implementation of these algorithms makes it possible to overcome the difficulties of 3D real-time imaging.

**Table 3**

Frame rates expressed in frames-per-second reached with the different imaging algorithms as a function of the number of voxels. A cross indicates that reconstruction is not feasible due to lack of memory in the graphic card.

$N_x \times N_y \times N_z$	Total voxels	TFM	k-TFM	PWI	k-PWI
$12 \times 12 \times 24$	$3.5 \times 10^3$	17	13	115	83
$24 \times 24 \times 48$	$2.8 \times 10^4$	3 <sup>a</sup>	13	115	81
$48 \times 48 \times 96$	$2.2 \times 10^5$	×	6	6 <sup>a</sup>	69
$88 \times 88 \times 176$	$1.3 \times 10^6$	×	1 <sup>a</sup>	×	52
$188 \times 188 \times 376$	$1.3 \times 10^7$	×	×	×	2 <sup>a</sup>

<sup>a</sup>Indicates that the associated reconstruction is performed with the maximum possible number of voxels.

## 5. Conclusion

In this paper, we have presented a way to perform fast and memory-efficient 3D imaging with matrix arrays. Two types of acquisition have been investigated: the first consists in the transmission of spherical waves by exciting the elements one by one, and the second uses incident plane waves where the elements are all excited in parallel with delay laws. In each case, we have presented the theory of the imaging method in the Fourier domain and demonstrated a significant decrease of the algorithmic complexity compared to the equivalent method operating in the time domain. In addition, the Fourier-domain methods have been improved in terms of required memory space, which makes it possible to compute 3D images with many more voxels in comparison with the implementation usually adopted in the literature. The four methods, namely TFM, k-TFM, PWI and k-PWI, have been evaluated experimentally using a 256-channel Vantage (Verasonics) system and parallel computations on graphic card. The imaged sample is a stainless steel block elaborated by additive manufacturing containing a 3D network of porosities of 0.8 mm diameter and the probe used is a  $16 \times 16$  matrix array at 5 MHz.

In terms of required memory space, it has been shown that for an image composed of  $10^8$  voxels, the k-TFM algorithm requires 80 times less memory than TFM while k-PWI 60 times less than PWI. The gain in frame rate depends strongly on the number of voxels. For an image with  $2.2 \times 10^5$  voxels, it has been shown that the frame rate is 11 times higher for k-PWI compared to PWI. For k-TFM, the frame rate is 4 times higher compared to TFM for an image with  $2.8 \times 10^4$  voxels. These results show that the use of imaging algorithms in the Fourier domain is a relevant approach for real-time 3D imaging and could improve the performance of NDT imaging systems in terms of frame rate and maximum number of voxels. The comparison of experimental 3D images formed in the time and frequency domains confirmed the theory: the faster amplitude decay with depth and the greater sensitivity to noise of the Fourier-domain algorithms lead to lower values of SNR compared to time-domain methods, in particular for defects far from the array. Further theoretical and experimental work is needed to better understand the origin of this attenuation and sensitivity to noise, which is specific to the Fourier domain algorithms. Future work will focus on finding methods to correct these effects using specific spatio-temporal filters.

## Declaration of competing interest

The authors declare that they have no known competing financial interests or personal relationships that could have appeared to influence the work reported in this paper.

## Acknowledgments

The authors would like to thank the team in charge of the Additive Manufacturing Hub (AFH) platform hosted at CEA for the elaboration of the stainless steel sample with spherical porosities.

## Appendix A. Imaging equation for a water–steel interface

The theoretical background presented in the paper considers a matrix array directly in contact with the specimen. It is common to carry out an “immersion” control where the probe is placed in water at a certain distance above the sample. The water height, noted  $h$ , is taken into account differently depending on the type of algorithm used.

For the time-domain algorithms, the calculation of the delay corresponding to the direct path of the wave is adapted. For TFM, the image amplitude can be expressed as

$$I_{\text{TFM}}(\mathbf{r}) = \left| \sum_{\mathbf{u} \in \mathcal{U}} \sum_{\mathbf{v} \in \mathcal{V}} s \left( \mathbf{u}, \mathbf{v}, \frac{\|\mathbf{h}_v - \mathbf{r}\| + \|\mathbf{h}_u - \mathbf{r}\|}{c} + \frac{\|\mathbf{v} - \mathbf{h}_v\| + \|\mathbf{u} - \mathbf{h}_u\|}{\tilde{c}} \right) \right| \quad (33)$$

where  $\tilde{c}$  is the phase velocity in water and the vectors  $\mathbf{h}_v$  and  $\mathbf{h}_u$  locate the impact points on the surface for the incident path and outgoing path, respectively [9]. The vectors  $\mathbf{h}_v$  and  $\mathbf{h}_u$  are computed by minimizing the time of flight while respecting Fermat's principle. Likewise, the image amplitude for PWI is expressed as

$$I_{\text{PWI}}(\mathbf{r}) = \left| \sum_{\mathbf{u} \in \mathcal{U}} \sum_{m \in \mathcal{M}} s_m \left( \mathbf{u}, \frac{(\mathbf{r} - \mathbf{h}_m) \cdot \mathbf{e}_m + \|\mathbf{h}_u - \mathbf{r}\|}{c} + \frac{\mathbf{h}_m \cdot \tilde{\mathbf{e}}_m + \|\mathbf{h}_u - \mathbf{r}\|}{\tilde{c}} + \tau_m \right) \right|, \quad (34)$$

where

$$\mathbf{h}_m = \begin{pmatrix} x - (z - h) \tan \theta_m \cos \phi_m \\ y - (z - h) \tan \theta_m \sin \phi_m \\ h \end{pmatrix},$$

locates the impact point on the surface of the incident plane wave and

$$\tilde{\mathbf{e}}_m = (\sin \tilde{\theta}_m \cos \phi_m, \sin \tilde{\theta}_m \sin \phi_m, \cos \tilde{\theta}_m)^T$$

with  $\tilde{\theta}_m = \arcsin\left(\frac{\tilde{c}}{c} \sin \theta_m\right)$  is the normal vector of the plane wavefront in water.

For the Fourier-domain algorithms, we use an idea developed by Skjeltvareid et al. [34]. The spectra which can be obtained with a control in direct contact are extrapolated from the spectra obtained in immersion. This allows to apply the Fourier-domain algorithms presented in this paper without any modification. The idea is to apply a phase shift to the spectra of recorded signals corresponding to the inverse propagation in water. For k-TFM, we multiply  $\hat{S}$  by the phase factor

$$\exp\left(ih \left( \sqrt{\tilde{k} - k_v} + \sqrt{\tilde{k} - k_u} \right)\right),$$

where  $\tilde{k} = \omega/\tilde{c}$  is the wavenumber corresponding to the propagation in water. The first term in exponential corresponds to the first propagation in water, just after emission, and the second term corresponds to the second propagation in water, from the surface to the receivers. For k-PWI, we multiply  $\hat{S}_m$  by the phase factor

$$\exp\left(ih \left( \tilde{k} \cos \hat{\theta}_m + \sqrt{\tilde{k} - k_u} \right)\right),$$

where the first term in exponential corresponds to the propagation in water of the plane wave. These operations provide a good approximation of the recorded data spectra that we would have obtained with a contact control.

## Appendix B. Derivation of the reflector distributions

In the following, the expressions of the distribution of point-like reflectors are derived for the four imaging methods following the idea proposed in [33] for the divergent waves emissions and adapted in [16] to plane waves emissions. The objective is to obtain expressions in the

form of integral over the same variables for both types of acquisition in order to compare the theoretical image amplitudes.

The isotropic point-like reflector distribution obtained with TFM at the point  $\mathbf{r}$  is expressed as

$$g_{\text{TFM}}(\mathbf{r}) = \iiint G_{\text{TFM}}(\mathbf{r}, \mathbf{u}, \mathbf{v}, k) \, d\mathbf{u}d\mathbf{v}dk. \quad (35)$$

where  $G_{\text{TFM}}(\mathbf{r}, \mathbf{u}, \mathbf{v}, k) = S(\mathbf{u}, \mathbf{v}, k)e^{ik(\|\mathbf{r}-\mathbf{v}\|+\|\mathbf{r}-\mathbf{u}\|)}$ . Using Eq. (5), the reflector distribution at the point  $\mathbf{r}$  obtained for k-TFM can be expressed as

$$g_{k\text{-TFM}}(\mathbf{r}) = \int \dots \int K_u K_v e^{i(k_u(\mathbf{r}-\mathbf{u})+k_v(\mathbf{r}-\mathbf{v})+(K_u+K_v)z)} S(\mathbf{u}, \mathbf{v}, k) \, d\mathbf{k}_u d\mathbf{k}_v d\mathbf{u}d\mathbf{v}dk. \quad (36)$$

To obtain an expression comparable to Eq. (35), the integral

$$J(\mathbf{r}, \mathbf{w}, k) = \int K_w e^{i(k_w(\mathbf{r}-\mathbf{w})+K_w z)} \, d\mathbf{k}_w \quad (37)$$

must be calculated. An asymptotic expression of the integrals of the form

$$L(\alpha) = \iint f(k_1, k_2) e^{i\alpha q(k_1, k_2)} \, dk_1 dk_2 \quad (38)$$

can be derived for  $\alpha \rightarrow \infty$  using the stationary phase method [35,36]. The result is given by

$$L(\alpha) \underset{\alpha \rightarrow \infty}{\sim} \frac{2\pi e^{i(\alpha q(k_1^*, k_2^*) + \sigma \frac{\pi}{4})}}{\alpha \sqrt{|\det(Q(k_1^*, k_2^*))|}} f(k_1^*, k_2^*), \quad (39)$$

where  $(k_1^*, k_2^*)$  is a stationary point of  $q$ , i.e., satisfying  $\nabla q(k_1^*, k_2^*) = 0$ ,  $Q$  is the Hessian matrix of  $q$  and  $\sigma = \text{sign}(\det(Q(k_1^*, k_2^*)))$ . Thus, by setting  $\alpha = kz$ ,  $f(k_{w_1}, k_{w_2}) = K_w$  and

$$q(k_{w_1}, k_{w_2}) = \frac{k_{w_1}(x-w_1) + k_{w_2}(y-w_2)}{kz} + \frac{K_w}{k}, \quad (40)$$

an asymptotic expression of integral in Eq. (37) can be obtained for  $kz \rightarrow \infty$ , which is given by

$$J(\mathbf{r}, \mathbf{w}, k) \underset{kz \rightarrow \infty}{\sim} A \frac{k^2 z^2}{\|\mathbf{r}-\mathbf{w}\|^3} e^{ik\|\mathbf{r}-\mathbf{w}\|} \quad (41)$$

with  $A$  a complex constant. The integrals over  $\mathbf{k}_u$  and  $\mathbf{k}_v$  in Eq. (36) can be evaluated for  $kz \rightarrow \infty$  using the result given in Eq. (41). The corresponding asymptotic expression is given by

$$g_{k\text{-TFM}}(\mathbf{r}) \underset{kz \rightarrow \infty}{\sim} A^2 \iiint \frac{k^4 \cos^2 \beta(\mathbf{r}, \mathbf{u}) \cos^2 \beta(\mathbf{r}, \mathbf{v})}{\|\mathbf{r}-\mathbf{u}\| \|\mathbf{r}-\mathbf{v}\|} G_{\text{TFM}}(\mathbf{r}, \mathbf{u}, \mathbf{v}, k) \, d\mathbf{u}d\mathbf{v}dk \quad (42)$$

with  $\beta(\mathbf{r}, \mathbf{w}) = \arccos\left(\frac{z}{\|\mathbf{r}-\mathbf{w}\|}\right)$  the angle at which the point  $\mathbf{r}$  is seen from the element positioned at  $\mathbf{w}$ . This expression is valid for the points  $\mathbf{r}$  sufficiently far away from the array, i.e. for  $z \gg \lambda$ .

The reflector distribution obtained with PWI for one plane wave emitted in the direction  $\mathbf{e}_m$  at the point  $\mathbf{r}$  is expressed as

$$g_{\text{PWI}}(\mathbf{r}) = \iint G_{\text{PWI}}(\mathbf{r}, \mathbf{u}, k) \, d\mathbf{u}dk. \quad (43)$$

where  $G_{\text{PWI}}(\mathbf{r}, \mathbf{u}, k) = S_m(\mathbf{u}, k)e^{ik(\mathbf{r} \cdot \mathbf{e}_m + \|\mathbf{r}-\mathbf{u}\|)}$ . Using Eq. (10), the reflector distribution obtained for k-PWI at the point  $\mathbf{r}$  is expressed as

$$g_{k\text{-PWI}}(\mathbf{r}) = \iiint K_u e^{i(k_r \mathbf{e}_m + \mathbf{k}_u \cdot (\mathbf{r}-\mathbf{u}) + K_u z)} S(\mathbf{u}, \mathbf{v}, k) \, d\mathbf{k}_u d\mathbf{u}d\mathbf{v}dk. \quad (44)$$

In the same way than for k-TFM, the integral over  $\mathbf{k}_u$  in Eq. (44) can be evaluated for  $kz \rightarrow \infty$  using result in Eq. (41) to obtain the following expression

$$g_{k\text{-PWI}}(\mathbf{r}) \underset{kz \rightarrow \infty}{\sim} A \iint \frac{k^2 \cos^2 \beta(\mathbf{r}, \mathbf{u})}{\|\mathbf{r}-\mathbf{u}\|} G_{\text{PWI}}(\mathbf{r}, \mathbf{u}, \mathbf{v}, k) \, d\mathbf{u}dk. \quad (45)$$

## References

- [1] M. Sutcliffe, M. Weston, B. Dutton, P. Charlton, K. Donne, Real-time full matrix capture for ultrasonic non-destructive testing with acceleration of post-processing through graphic hardware, *NDT E Int.* 51 (2012) 16–23, <http://dx.doi.org/10.1016/j.ndteint.2012.06.005>.
- [2] M. Lewandowski, M. Walczak, B. Witek, J. Rozbicki, T. Steifer, A GPU-based portable phased-array system with full-matrix capture, in: *IEEE Int. Ultrason. Symp.*, 2018, pp. 1–3, <http://dx.doi.org/10.1109/ULTSYM.2018.8579964>.
- [3] B.W. Drinkwater, P.D. Wilcox, Ultrasonic arrays for non-destructive evaluation: A review, *NDT E Int.* 39 (7) (2006) 525–541, <http://dx.doi.org/10.1016/j.ndteint.2006.03.006>.
- [4] C. Holmes, B.W. Drinkwater, P.D. Wilcox, Post-processing of the full matrix of ultrasonic transmit–receive array data for non-destructive evaluation, *NDT E Int.* 38 (8) (2005) 701–711, <http://dx.doi.org/10.1016/j.ndteint.2005.04.002>.
- [5] C.J.L. Lane, T.K. Dunhill, B.W. Drinkwater, P.D. Wilcox, 3D ultrasonic inspection of anisotropic aerospace components, *Insight: Non-Destr. Test. Cond. Monit.* 52 (2) (2010) 72–77, <http://dx.doi.org/10.1784/insi.2010.52.2.72>.
- [6] S. Kitazawa, N. Kono, A. Baba, Y. Adachi, M. Odakura, O. Kikuchi, Three-dimensional visualisation and evaluation techniques for volumetrically scanned data of ultrasonic phased arrays, *Insight: Non-Destr. Test. Cond. Monit.* 52 (4) (2010) 201–205, <http://dx.doi.org/10.1784/insi.2010.52.4.201>.
- [7] J. Brizuela, J. Camacho, G. Cosarinsky, J.M. Iriarte, J.F. Cruza, Improving elevation resolution in phased-array inspections for NDT, *NDT E Int.* 101 (2019) 1–16, <http://dx.doi.org/10.1016/j.ndteint.2018.09.002>.
- [8] G. Montaldo, M. Tanter, J. Bercoff, N. Benech, M. Fink, Coherent plane-wave compounding for very high frame rate ultrasonography and transient elastography, *IEEE Trans. Ultrason. Ferroelectr. Freq. Control* 56 (3) (2009) 489–506, <http://dx.doi.org/10.1109/TUFFC.2009.1067>.
- [9] L. Le Jeune, S. Robert, E. Lopez Villaverde, C. Prada, Plane wave imaging for ultrasonic non-destructive testing: Generalization to multimodal imaging, *Ultrasonics* 64 (2016) 128–138, <http://dx.doi.org/10.1016/j.ultras.2015.08.008>.
- [10] L. Merabet, S. Robert, C. Prada, The multi-mode plane wave imaging in the Fourier domain: Theory and applications to fast ultrasound imaging of cracks, *NDT E Int.* 110 (2020) 102171, <http://dx.doi.org/10.1016/j.ndteint.2019.102171>.
- [11] L. Le Jeune, S. Robert, C. Prada, Plane wave imaging for ultrasonic inspection of irregular structures with high frame rates, *AIP Conf. Proc.* 1706 (1) (2016) 020010, <http://dx.doi.org/10.1063/1.4940456>.
- [12] R.K. Rachev, P.D. Wilcox, A. Velichko, K.L. McAughey, Plane wave imaging techniques for immersion testing of components with nonplanar surfaces, *IEEE Trans. Ultrason. Ferroelectr. Freq. Control* 67 (7) (2020) 1303–1316, <http://dx.doi.org/10.1109/TUFFC.2020.2969083>.
- [13] M. Ducouso, F. Reverdy, Real-time imaging of microcracks on metallic surface using total focusing method and plane wave imaging with Rayleigh waves, *NDT E Int.* 116 (2020) 102311, <http://dx.doi.org/10.1016/j.ndteint.2020.102311>.
- [14] R.H. Stolt, Migration by Fourier transform, *Geophysics* 43 (1) (1978) 23–48, <http://dx.doi.org/10.1190/1.1440826>.
- [15] D. Garcia, L.L. Tarnec, S. Muth, E. Montagnon, J. Porée, G. Cloutier, Stolt's f-k migration for plane wave ultrasound imaging, *IEEE Trans. Ultrason. Ferroelectr. Freq. Control* 60 (9) (2013) 1853–1867, <http://dx.doi.org/10.1109/TUFFC.2013.2771>.
- [16] L. Merabet, S. Robert, C. Prada, 2-d and 3-D reconstruction algorithms in the Fourier domain for plane-wave imaging in nondestructive testing, *IEEE Trans. Ultrason. Ferroelectr. Freq. Control* 66 (4) (2019) 772–788, <http://dx.doi.org/10.1109/TUFFC.2019.2895995>.
- [17] L. Merabet, S. Robert, C. Prada, Development and evaluation of f-k migration methods for fast ultrasonic imaging in solids, in: *IEEE Int. Ultrason. Symp.*, 2016, pp. 1–4, <http://dx.doi.org/10.1109/ULTSYM.2016.7728685>.
- [18] G. Franceschetti, G. Schirrinzi, A SAR processor based on two-dimensional FFT codes, *IEEE Trans. Aerosp. Electron. Syst.* 26 (2) (1990) 356–366, <http://dx.doi.org/10.1109/7.53462>.
- [19] H. Callow, M. Hayes, P. Gough, Wavenumber domain reconstruction of SAR/SAS imagery using single transmitter and multiple-receiver geometry, *Electron. Lett.* 38 (7) (2002) 336–338, <http://dx.doi.org/10.1049/el:20020219>.
- [20] A.J. Hunter, B.W. Drinkwater, P.D. Wilcox, The wavenumber algorithm for full-matrix imaging using an ultrasonic array, *IEEE Trans. Ultrason. Ferroelectr. Freq. Control* 55 (11) (2008) 2450–2462, <http://dx.doi.org/10.1109/TUFFC.952>.
- [21] J. Cheng, J. Yu Lu, Extended high-frame rate imaging method with limited-diffraction beams, *IEEE Trans. Ultrason. Ferroelectr. Freq. Control* 53 (5) (2006) 880–899, <http://dx.doi.org/10.1109/TUFFC.2006.1632680>.
- [22] Z. Zhuang, J. Zhang, G. Lian, B.W. Drinkwater, Comparison of time domain and frequency-wavenumber domain ultrasonic array imaging algorithms for non-destructive evaluation, *Sensors* 20 (17) (2020) 4951, <http://dx.doi.org/10.3390/s20174951>.
- [23] E.L. Villaverde, S. Robert, C. Prada, Ultrasonic imaging in highly attenuating materials with Hadamard codes and the decomposition of the time reversal operator, *IEEE Trans. Ultrason. Ferroelectr. Freq. Control* 64 (9) (2017) 1336–1344, <http://dx.doi.org/10.1109/TUFFC.2017.2690499>.

- [24] W.C. Chew, *Waves and Fields in Inhomogeneous Media*, IEEE Press, New York, 1995.
- [25] W. Harlan, *Avoiding interpolation artifacts in stolt migration*, *Stanford Explor. Proj.* 30 (1982) 103–110.
- [26] P. Kruizinga, F. Mastik, N. de Jong, A.F. van der Steen, G. van Soest, Plane-wave ultrasound beamforming using a nonuniform fast fourier transform, *IEEE Trans. Ultrason. Ferroelectr. Freq. Control* 59 (12) (2012) 2684–2691, <http://dx.doi.org/10.1109/TUFFC.2012.2509>.
- [27] Z. Li, J. Wang, J. Wu, Q.H. Liu, A fast radial scanned near-field 3-D SAR imaging system and the reconstruction method, *IEEE Trans. Geosci. Remote Sens.* 53 (3) (2015) 1355–1363, <http://dx.doi.org/10.1109/TGRS.2014.2338396>.
- [28] Z. Li, J. Wang, Q.H. Liu, Interpolation-free stolt mapping for SAR imaging, *IEEE Geosci. Remote. Sens. Lett.* 11 (5) (2014) 926–929, <http://dx.doi.org/10.1109/LGRS.2013.2281847>.
- [29] C. Kim, H. Yin, A. Shmatok, B.C. Prorok, X. Lou, K.H. Matlack, Ultrasonic nondestructive evaluation of laser powder bed fusion 316L stainless steel, *Addit. Manuf.* 38 (2021) 101800, <http://dx.doi.org/10.1016/j.addma.2020.101800>.
- [30] X. Rayleigh, *Investigations in optics, with special reference to the spectroscope*, *Lond. Edinb. Dublin Philos. Mag. J. Sci.* 8 (49) (1879) 261–274, <http://dx.doi.org/10.1080/14786447908639684>.
- [31] N. Laroche, S. Bourguignon, E. Carcreff, J. Idier, A. Duclos, An inverse approach for ultrasonic imaging from full matrix capture data: Application to resolution enhancement in NDT, *IEEE Trans. Ultrason. Ferroelectr. Freq. Control* 67 (9) (2020) 1877–1887, <http://dx.doi.org/10.1109/TUFFC.2020.2990430>.
- [32] S.C. Mondal, P.D. Wilcox, B.W. Drinkwater, Design and evaluation of two dimensional phased array ultrasonic transducers, *AIP Conf. Proc.* 760 (1) (2005) 899–905, <http://dx.doi.org/10.1063/1.1916769>.
- [33] A. Velichko, P.D. Wilcox, An analytical comparison of ultrasonic array imaging algorithms, *J. Acoust. Soc. Am.* 127 (4) (2010) 2377–2384, <http://dx.doi.org/10.1121/1.3308470>.
- [34] M.H. Skjelvareid, T. Olofsson, Y. Birkelund, Y. Larsen, Synthetic aperture focusing of ultrasonic data from multilayered media using an omega-K algorithm, *IEEE Trans. Ultrason. Ferroelectr. Freq. Control* 58 (5) (2011) 1037–1048, <http://dx.doi.org/10.1109/TUFFC.2011.1904>.
- [35] C.M. Bender, S.A. Orszag, *Advanced Mathematical Methods for Scientists and Engineers I: Asymptotic Methods and Perturbation Theory*, Springer-Verlag, New York, 1999.
- [36] L. Hörmander, *The Analysis of Linear Partial Differential Operators I: Distribution Theory and Fourier Analysis*, second ed., Springer-Verlag, Berlin Heidelberg, 2003.